Disentangling seasonal signals in Holocene climate trends by satellite-model-proxy integration

B. Schneider,[1] G. Leduc,[1] and W. Park,[2]

B. Schneider, Institute of Geosciences, University of Kiel, Ludewig-Meyn-Str. 10, D-24118 Kiel, Germany. (bschneider@gpi.uni-kiel.de)

G. Leduc, Institute of Geosciences, University of Kiel, Ludewig-Meyn-Str. 10, D-24118 Kiel, Germany.

W. Park, Leibniz Institute of Marine Sciences, Düsternbrooker Weg 20, D-24105 Kiel, Germany.

[1]Institute of Geosciences, University of Kiel, Ludewig-Meyn-Str. 10, D-24118 Kiel, Germany.

[2]Leibniz Institute of Marine Sciences, Düsternbrooker Weg 20, D-24105 Kiel, Germany.

Past sea surface temperatures (SSTs) are routinely estimated from organic and inorganic remains of fossil phytoplankton or zooplankton organisms, recovered from sea floor sediments. Potential seasonal biases of paleo proxies were intensely studied in the past, however, even for the two most commonly used paleo proxies for SST, $U_{37}^{K'}$ and Mg/Ca ratios, a clear global picture does not yet exist. In the present study we combine Holocene SST trends derived from $U_{37}^{K'}$ and Mg/Ca ratios with results from idealized climate model simulations forced by changes in the orbital configuration, which represents the major climate driver over the last 10 kyrs. Such changes cause a spatio-temporal redistribution of incoming solar radiation resulting in a modulation of amplitude and phasing of the seasonal cycle. Considering that the climate signal recorded by a plankton-based paleo proxy may be affected by the seasonal productivity cycle of the respective organism, we use the modern relationship between SST and marine net primary production (NPP), both obtained from satellite observations, to calculate a seasonality index (SI) as an independent constraint to link modeled SST trends with proxy data. Although the climate model systematically underestimates Holocene SST trends, we find that seasonal productivity peaks of the phytoplankton-based $U_{37}^{K'}$ result in a preferential registering of the warm (cold) season in high (low) latitudes, as it was expected from the SI distribution. The overall smoother trends from the zooplankton-derived Mg/Ca-SSTs suggest a more integrated signal over longer time averages, which may also carry a seasonal bias, but the spatial

pattern is less clear. Based on our findings, careful multi-proxy approaches can actually go beyond the reconstruction of average climate trends, specifically allowing to resolve the evolution of seasonality.

1. Introduction

Paleo proxies are routinely used to reconstruct past climate conditions. However, they provide only indirect estimates of past environmental conditions, so that attributing a proxy to a certain climate property [Mann et al., 2009] and the sensitivity of a proxy to internal climate variability [Legrande and Schmidt, 2009] are important issues to be considered when interpreting proxy records. In oceanic environments past sea surface temperatures (SSTs) are commonly estimated from marine sediment cores using either the alkenone unsaturation index $U_{37}^{K'}$ or the Mg/Ca ratio of planktonic foraminifera tests, measured on fossil marine phytoplankton and zooplankton remains, respectively. A potential seasonal bias of paleo proxies has often been acknowledged to result either from the productivity cycle of plankton organisms [Fraile et al., 2009a; Fraile et al., 2009b; Oppo et al., 2009; Prahl et al., 2009; Conte et al., 2006; Ternois et al., 1998; Sikes et al., 1997; Sonzogni et al., 1997; Prahl and Wakeham, 1987; Mix et al., 1986] or from seasonally varying sensitivity of the physical climate system to climate change [Laepple and Lohmann, 2009; Huybers and Denton, 2008].

Recently, a global compilation of existing Holocene SST reconstructions based on $U_{37}^{K'}$ and Mg/Ca has identified several regions with uniform trends for each proxy, but systematically diverging results between both proxies [Leduc et al., 2010]. These results strongly support the robustness of each of the proxy organisms, while suggesting that both proxies probably differ in their sensitivity to climate change. In the present study we use the Holocene SST data compilation for comparison with results from an atmosphere ocean general circulation model (AOGCM; Kiel Climate Model; KCM) [Park and Latif, 2008;

Park et al., 2009] that was adapted to changes in the orbital configuration that occurred over the Holocene ($\sim$ 10 kyr BP to present). Even though other factors may also operate [Renssen et al., 2009], we assume that astronomical forcing provides a first order mechanism shaping the proxy records considered here. Consequently, the Holocene is an ideal period to test potential seasonal effects on proxy records, as the major climate forcing is most effectively modulating the seasonal cycle.

Our aim is to provide a global perspective on potential seasonal preferences of the two most commonly used paleo proxies for SST ($U_{37}^{K'}$ and Mg/Ca), which would have implications for the interpretation of paleo climate records as well as for proxy calibration. We analyze how a signal of external climate forcing is modulated by cascading through the dynamically responding systems such as atmosphere, surface ocean, and marine biology, until ultimately shaping the respective proxy record (Figure 1). The sensitivity of the physical climate system is represented by the KCM. A combination of satellite-derived data of modern marine net primary production (NPP) [Behrenfeld et al., 2006] and SST [Reynolds et al., 2007] is used to identify regions with pronounced seasonal variability in both climate and plankton productivity, which would result in enhanced seasonal sensitivity of plankton-based paleo proxies. The independent link of model results and proxy records by satellite data allows us on the one hand to derive a conceptual model for the climate signal that is expected to be contained in the paleo data. On the other hand, a better knowledge of the climate signal ultimately captured by the data allows a better quantification of model misfits. We hypothesize that the same external climate forcing

has a different impact on various proxy organisms, resulting in systematically divergent climate trends as shown by Leduc et al. [2010].

2. Materials and Methods

2.1. Model simulations of the physical climate system responding to orbital forcing

A series of quasi steady-state simulations is conducted with a fully coupled atmosphere ocean general circulation model (AOGCM), the Kiel Climate Model (KCM), representing three time intervals during the Holocene (preindustrial, 6 kyrs BP, 9.5 kyrs BP). The model includes the atmospheric component ECHAM5 [Roeckner et al., 2003] with a T31 resolution (3.75^ox3.75^o) horizontally and 19 levels vertically. The ocean model OPA9 [Madec, 2008] is on a 2-degree Mercator mesh with enhanced meridional resolution of 0.5 degrees in the equatorial region, and 31 vertical levels which are increasing in thickness from 10 m in the upper 100 m to 500 m at depth. The sea-ice model LIM2 [Fichefet and Morales Maqueda, 1997] is coupled to OPA9 and run on the ocean grid. The ocean and atmosphere models are coupled via the coupler OASIS3 [Valcke, 2003]. The model does not use any flux correction, and it has already shown to realistically reproduce present day climate and ocean circulation [Park and Latif, 2008]. Particularly in the tropical Pacific the model yields reasonable results with a clear annual SST cycle in the east, a semi-annual SST cycle in the west and a zonal SST gradient of about 2.7^oC [Park et al., 2009]. Furthermore, the model reproduces the east-to-west propagation of SST anomalies and it exhibits ENSO events distinctly different from a too regular biennial cycle with frequencies peaking between 3-4 years. A more detailed description of the model setup

and results of the model for the modern situation are given in Park and Latif [2008] and Park et al. [2009].

In the present study three time-slice experiments are performed with prescribed orbital configurations for the parameters eccentricity, obliquity and precession, according to the respective time periods of preindustrial (0K), mid-Holocene (6K) and early Holocene (9.5K), following the standard protocol of the Paleo-Modeling Intercomparison Project (PMIP) [Joussaume and Taylor, 1995; Braconnot et al., 2008]. This approach is rather a sensitivity test of climate models to changes in orbital configuration, as it neglects other forcing factors, such as greenhouse gases and ice sheets. However, these are assumed to be of minor importance compared to the orbital forcing, and some potential effects of this neglect will be discussed later in this work. Adapting the orbital parameters results in a spatio-temporal redistribution of solar insolation at the top of the atmosphere with a modified signal arriving at the sea surface (Figure 1a-b). All simulations are initialized with the World Ocean Atlas (WOA) climatology [Conkright et al., 2002] for temperature and salinity and are spun up over 500 years. Another 500 years of model integrations provide stable climate conditions that are used for the analysis. Climatological mean SSTs are calculated for all simulations, and Holocene SST trends are derived as the differences between the different time slices.

2.2. Paleo proxy data for Holocene SST trends

Paleotemperature proxy data for the model-data comparison of Holocene SST trends are taken from a data compilation that combines SST reconstructions from $U_{37}^{K'}$ and Mg/Ca (Figure 2)[Leduc et al., 2010; Kim et al., 2004]. All included data sets have been published

before, individually. Alkenones are C37 (ketones) organic carbon molecules synthesized by coccolithophorids, and their degree of unsaturation provided by the $U_{37}^{K'}$ unsaturation index is commonly used as an indicator for sea surface temperature [Conte et al., 2006; Prahl and Wakeham, 1987]. Additionally, Mg/Ca ratios measured on planktonic foraminifera tests are also used as temperature indicators [Nürnberg et al., 1996; Regenberg et al., 2009]. The corresponding Holocene SST trends are calculated as the difference between the first and the last 1000 years in the records and assumed to be linear (Tables 1 and 2). While the $U_{37}^{K'}$ data is obtained from the organic remains of the coccolithophorid species *Emilianiahuxleyi* and *Geophyrocapsaoceanica*, the individual zooplankton species on which the Mg/Ca data is measured are listed in Table 2. A detailed description of the data set is given by Leduc et al., [2010].

2.3. Marine biogeochemical system

For the evaluation of the observed modern relationship between SST and phytoplankton productivity climatological values for net primary production (NPP) [Behrenfeld et al., 2006] averaged over the years 1997-2006 are combined with SST data from the same period [Reynolds et al., 2007], both derived from independent satellite measurements. A seasonality index (SI; Figure 3a) based on the seasonal amplitudes of SST (K) and NPP (gC m^{-2} yr^{-1}) including their phase relationship is calculated as

$$SI = \left(\frac{NPP_{amp}}{NPP_{ave}}\right)_{norm} \cdot \left(\frac{SST_{amp}}{SST_{ave}}\right)_{norm} \cdot sign(R) \quad (1)$$

where the relative amplitudes of NPP and SST at each grid point are normalized by the respective global average value to avoid the index to be dominated by NPP variability.

The regression coefficient R is determined by linearly regressing SST with NPP over the 12 months of the climatologies, and its sign (positive or negative; ± 1) is used to distinguish areas with positive and negative SST-NPP relationships. The absolute value of R is not used here, as it is not important for the existence of seasonal signals in proxy organisms. It may, however, be important for the calibration of paleo proxies, and areas where the absolute value of R is larger than 0.8 are contoured in Figure 3a. Those areas where the seasonal amplitude of SST is below 2^oC are also marked (dashed lines), as here the sensitivity of the proxies may be too low to be affected by seasonality.

To investigate potential interactions among different phytoplankton species, which can not be separated by the satellite data used, but may affect the climate signal stored in paleo proxies, results from a 3000 year spinup of the IPSL-PISCES marine biogeochemical model are used [Gehlen et al., 2006]. This model couples climate and the marine carbon cycle for the preindustrial situation, simulating two phytoplankton size classes, which represent silicifying diatoms and to some extent calcite forming nanophytoplankton [Aumont et al. 2003]. The mentioned species interactions result from the competition for nutrients.

2.4. Filtering modeled SST trends

To isolate Holocene temperature trends from the model as they would most probably be registered by paleo proxies with a seasonal preference, we apply several filters to the model results that are used to mimic the respective proxy sensitivity, relying on the modern template of the NPP-SST relationship as given in Figure 3a. By comparing different filtered trends with the proxy data, it can be distinguished which filter is yielding the best match.

T-ANN

The filter T-ANN uses the annual mean SST to derive the trends, which means it weights all months of the year, equally. This filter is considered as the reference for comparison with all other filtered trends, as it is based on the assumption that paleo proxies of SST represent annual mean climate conditions. This assumption is often made in the absence of a clear indication for a distinct seasonal signal.

SI-WEIGHT

Exploiting the information given in Figure 3a the SI-weighted SST-trend (SI-WEIGHT) is computed from the model results by weighting each month by W:

$$W = \frac{NPP - NPP_{min}}{NPP_{amp}} \cdot \frac{SST - SST_{min}}{SST_{amp}}, \tag{2}$$

when the correlation between SST and NPP is positive (R>0), and

$$W = \frac{NPP - NPP_{min}}{NPP_{amp}} \cdot \frac{SST_{max} - SST}{SST_{amp}} \tag{3}$$

when the correlation is negative (R<0). The SI-WEIGHT trend is then calculated as

$$SI - WEIGHT = \frac{\sum W_i \cdot \Delta SST_i}{\sum W_i}, \tag{4}$$

where ΔSST is the SST difference (trend) between the time slices. This filter implies that the modern NPP-SST relationship is also valid for other time periods during the Holocene. Furthermore, it implicitly assumes that the flux of material toward depth is

pulsed [Bijma et al. 2001], and that temperature next to NPP exerts a control on the amount of material exported relative to NPP [Laws et al., 2000].

T-MAX, T-MIN

Taking into account the positive (negative) phase relationship between NPP and SST at high (low) latitudes (Figure 3a), the respective warmest (T-MAX) or coldest (T-MIN) month of the year is used to calculate the Holocene SST trends. Assuming that the plankton organisms keep their preference for the respective warmest or coldest months of the year, both filters consider possible phase shifts in the seasonal cycle of SST, which may have occurred over the Holocene. Consequently, the respective maximum/minimum temperatures do not necessarily have to occur at the same months in the different Holocene time periods investigated here.

3. Results and Discussion

3.1. Prerequisites for seasonal signals in paleo proxy records

Considering that an organism at the origin of a paleo proxy may carry a seasonally weighted SST signal requires that the seasonal cycles of both proxy productivity and SST exhibit sufficiently large amplitudes compared to background values [Huybers and Wunsch, 2003]. In fact, the seasonality index (SI) shows a clear latitudinal pattern with a strong positive SST-NPP relationship at high latitudes and a weaker negative one in the low-latitude permanently stratified ocean (Figure 3a) [Behrenfeld et al., 2006]. The higher the value of the SI the more the climate signal is focused on a particular season or month. Given that marine net primary production (NPP) represents the productivity of a $U_{37}^{K'}$-SST proxy, a direct implication provided by the SI is that $U_{37}^{K'}$ would rather reflect warm

(cool) periods over the year at high (low) latitudes. A pronounced phase relationship between SST and NPP with correlation coefficients higher than 0.8 (or lower than -0.8) is found for roughly one third of the surface ocean (contour lines in Figure 3a). A high absolute value of R indicates that the preferentially recorded temperature deviates more strongly from the annual mean, which would be important for the calibration of proxy indices from core tops against modern SST.

The detected latitudinal SI pattern is not due to physiological effects, but rather arising from water column dynamics. At high latitudes phytoplankton productivity is mainly light limited because of strong vertical mixing during winter, while surface ocean warming and enhanced stratification in summer results in phytoplankton blooms. At low latitudes the surface ocean is permanently stratified and nutrient depleted, thus deep mixing events associated with cooler temperatures provide new nutrients from below, fuelling phytoplankton productivity [Behrenfeld et al., 2006; Schneider et al., 2008]. Interestingly, the zonally averaged SI is higher in the Northern than in the Southern Hemisphere (Figure 3b), because iron next to light limits phytoplankton growth in the Southern Ocean [Martin et al., 1990; Schneider et al., 2008]. As iron is mostly provided by upwelling in the Southern Ocean [Blain et al., 2007], this provides a dampening effect on the SST-NPP relationship.

A seasonal signal in $U_{37}^{K'}$-based SST estimates, as suggested by the SI (Figure 3a), is supported by sediment trap data from the North Atlantic that are demonstrating a clear pattern of enhanced flux of the alkenone-producing coccolithophorid *Emilianiahuxleyi* during the warm (cold) season at high (low) latitudes [Bijma et al., 2001]. The negative

SI in the western Arabian Sea and the positive SI in the Bay of Bengal clearly match findings from sediment trap data where the highest flux of organic material occurs during the coldest (western Arabian Sea) and the warmest (Bay of Bengal) season, respectively [Sonzogni et al., 1997]. Studies calibrating the $U_{37}^{K'}$ unsaturation index against SST have pointed out this potential bias, but argued that the application of annual mean SSTs resulted in the highest correlations [Conte et al., 2006; Müller et al., 1998; Prahl and Wakeham, 1987]. However, this result can be due to pronounced spring or fall blooms occurring when the ambient SST may accidentally correspond to the annual mean [Bijma et al., 2001]. Similarly, sediment trap data have shown that planktonic foraminifera species used to estimate Mg/Ca-based paleo SSTs may not always record annual mean conditions. For example, in the Panama Basin about 60% of the annual flux of the planktonic foraminifera *G.ruber*, occurred during boreal summer months [Thunell et al., 1983]. Taken together, sediment trap data from several locations support the potential for seasonal biases of paleo SST records derived from both phytoplankton ($U_{37}^{K'}$) and zooplankton (Mg/Ca).

3.2. Model-data comparison

Annual mean Holocene SST trends (preindustrial minus early Holocene) simulated by the model are largely reflecting the insolation forcing trend, with a clear warming at low latitudes, caused by the positive insolation anomaly due to decreased obliquity (Figure 3c). The same effect induces cooling at high latitudes, where the climate system is more susceptible to the respective summer season, when the mixed layer depth (MLD) is shallow and sea-ice cover at minimum [Laepple and Lohmann, 2009] (Figure 1c). As a result,

obliquity-forced cooling in the Northern Hemisphere is amplified by the precession-induced negative insolation anomaly during boreal summer. A late Holocene regional warming south of Iceland can be explained by an intensification of deep convection. In the Southern Ocean the expected cooling effect south of 45^oS is overcompensated by positive insolation forcing during austral summer (Figure 1).

Our results are consistent with other models simulating the climate of the Holocene, that have shown to be qualitatively in rough agreement with proxy reconstructions for SSTs derived from $U_{37}^{K'}$ [Voss and Mikolajewicz, 2001; Lorenz and Lohmann, 2004; Lorenz et al., 2006; Kim et al., 2004]. However, when our model results are superimposed with multi-proxy reconstructions there is still considerable disagreement in many places (Figure 3c). The KCM is generally underestimating $U_{37}^{K'}$-based SST trends, particularly at high latitudes, when annual mean SSTs are considered. Furthermore, modeled and observed SST trends are sometimes in opposite directions at mid-latitudes in the Southern Hemisphere. Finally, proxy-related divergent SST trends in the Northeast Atlantic and the Eastern Equatorial Pacific (EEP) [Leduc et al., 2010] cannot be resolved by a single model projection, and suggest that at least one of the proxies is probably not showing annual mean SST, but rather a seasonally affected SST signal.

3.3. Filtering the climate signal captured by proxy records

To explore the seasonal signal that is potentially recorded by proxy organisms, we use information provided by the SI (Figure 3a) to extract an SI-weighted SST trend from the model (Figure 3d). This approach goes beyond the study of Lorenz et al. [2006], who showed a stronger cooling over the Northern Hemisphere when displaying the tempera-

ture trend of the respective warmest month of the year, assuming that phytoplankton productivity peaks during summer. Given that high rates of NPP and subsequent export flux [Boyd and Trull, 2007], amplified by the seasonal cycle of SST, largely determine the climate signal embedded in $U_{37}^{K'}$, our SI-weighted Holocene SST trends are in better agreement with proxy data than annual mean modeled trends in many places, e.g. in the North Atlantic and the North Pacific (Figure 3d). The validity of the assumption of SI-WEIGHT, that the export of material is pulsed rather than continuous and controlled by both NPP and SST (see methods), is supported by a better agreement between SI-WEIGHT derived and reconstructed SST trends compared to SST trends weighted by the seasonal cycle of NPP alone or the month of maximum NPP (not shown).

According to Figure 3a, $U_{37}^{K'}$ would at first order register the warm (cool) season at high (low) latitudes, such that also the respective warmest and coldest months during the year can be used as filters for the model results (T-MAX, T-MIN). These two filters, as mentioned before, account for seasonal phase shifts in SST, which means temperature maxima and minima do not necessarily have to occur during the same months in the different time periods we investigate. In many places the resulting filtered SST trends get actually closer to the proxy data than those filtered by T-ANN (Figure 4). Clearly, SI-WEIGHT gets better results than T-ANN in most places for the $U_{37}^{K'}$ data. For 41 out of 54 locations from which $U_{37}^{K'}$ data exists, modeled and reconstructed trends are converging when considering the SI-weighted SST trends instead of annual mean values from the model. Although such a relationship was not a priori expected for Mg/Ca data, 13 out of 26 data points yield a better match for the SI-weighted SST trends, suggesting

that in some regions zooplankton organisms may undergo a seasonal cycle, potentially triggered by the seasonal cycle of their phytoplankton food source.

The multiple filtered SST trends allow to diagnose which filter is yielding the closest match, i.e. the lowest mismatch, with the data, for each proxy at each location. Here, the degree of improvement of a filtered SST trend compared to T-ANN can be expressed as the cost function, C:

$$C[\%] = \frac{abs(\Delta SST_{filter} - \Delta SST_{proxy})}{abs(\Delta SST_{T-ANN} - \Delta SST_{proxy})} \cdot 100, \quad (5)$$

which is the percent mismatch made by the respective filter relative to the mismatch resulting from the annual mean, with ΔSST representing the SST trends (filtered, data). The lower the value of C the better the match of the respective filter compared to T-ANN. Accordingly, $U_{37}^{K'}$ data exhibit a clear signal to represent the warm season (T-MAX) in high northern latitudes (Figure 5a), while at low latitudes T-MIN yields most often the best result. SI-WEIGHT is clearly dominant in the Indian Ocean, where sediment trap data have already shown that $U_{37}^{K'}$ derived SST signals strongly follow the seasonal cycle of plankton productivity [Sonzogni et al., 1997]. For only five out of 54 locations the annual mean SST (T-ANN) provides the best result for the $U_{37}^{K'}$ data. The same procedure applied to Mg/Ca data shows a less clear spatial pattern (Figure 5b). However, only for five out of 26 data points the annual mean is the best filter, and none of them is located in the Northern Hemisphere extratropics. This result indicates that in some regions Mg/Ca-derived SST trends may also be better approximated by seasonal subsampling. However, Mg/Ca data are even more sparse than $U_{37}^{K'}$ and the generally smoother Mg/Ca-trends,

compared to $U_{37}^{K'}$ [Leduc et al., 2010] suggest that Mg/Ca is probably integrating over longer time intervals than $U_{37}^{K'}$, which underlies more peaked productivity and downward flux [Bijma et al., 2001].

3.4. Effect of plankton interactions on proxy records

At certain locations, different SST trends for the early compared to the late Holocene may help to clarify the interpretation of proxy-related diverging SST trends. In the eastern equatorial Pacific (EEP) all $U_{37}^{K'}$ records agree on a constant warming trend, while Mg/Ca ratios exhibit no clear trend over the entire Holocene [Leduc et al., 2010]. When the Holocene period is split into the early (9.5 kyr to 6 kyr) and late (6 kyr to preindustrial) Holocene, an early cooling trend followed by a slight warming is often detected from Mg/Ca in the EEP.

The EEP exhibits a warm and stratified season in the boreal winter (JFM) and a cold upwelling season during boreal summer (JAS). The existence of a permanent cold tongue is a result of the local wind forcing that is driving continental and equatorial divergence of surface currents (Figure 6d, h, l), especially during boreal summer when the ITCZ is at its northernmost position. An expansion of the seasonal amplitude of SST in the EEP is manifested by a strong cooling of the upwelling season (JAS) during the early Holocene and a strong warming of the warm phase (JFM) during the late Holocene. This feature is partly driven by insolation changes (see insolation anomalies given in Figure 6), however, the co-existence of strong insolation anomalies together with relatively weak SST changes and vice versa indicates that ocean circulation change (equatorial and continental divergence/convergence) probably plays the more important role (Figure 6f, g,

i), sometimes in concert with the insolation changes (Figure 6a, c, e, j). Only for the late Holocene annual mean trends and the full Holocene boreal winter trends local insolation is dominating the SST signal (Figure 6b, i).

When overlaying model results with proxy data in the EEP, the $U_{37}^{K'}$ data are in good agreement with modeled SST trends for the boreal winter (JFM). In contrast, the Mg/Ca records are best represented by SI-weighted SST trends (Figure 5b), that are intermediate between annual mean and boreal summer trends (JAS; Figure 6). This systematic seasonal difference among the proxies could not be explained by a change in the vertical structure of the water column in our model-data comparison. Although in single cases the $U_{37}^{K'}$ record matches slightly better with subsurface temperature trends from the model (down to 35 m), it clearly remains the warm season that yields the best agreement with the proxy data. Also, Mg/Ca in some cases slightly better matches with subsurface temperature trends from the model trends (down to 200 m), while mostly the upwelling season or the annual mean trends are getting closest to the data. This largely supports the surface findings as shown in Figure 5b.

The fact that the $U_{37}^{K'}$ records benchmark the warm and stratified season during boreal winter (Figures 5a and 6i-k) is puzzling, since higher NPP is related to the cold season (Figure 3a). This paradox can be explained by the fact that here the alkenone-producing coccolithophorids are in competition with other phytoplankton species, in particular diatoms. The EEP is known to be strongly iron limited [Hutchins and Bruland, 1998]. As iron becomes available during the cold upwelling season, diatoms preferentially take up the nutrients, outcompeting other phytoplankton taxa such as coccolithophorids. In the

absence of any sediment trap studies resolving the seasonal dynamics of different phytoplankton species in the EEP, a marine biogeochemical model is used, which includes two phytoplankton functional types, representing diatoms and calcite forming nanophytoplankton (Figure 7) [Gehlen et al., 2006]. Both model and satellite data show a clear anti-phase relation of SST and NPP (Figure 3a and 7). The biogeochemical model also shows that there is a pronounced peak in the relative abundance of diatoms during the month of highest NPP (Figure 7), suggesting that small phytoplankton such as alkenone ($U_{37}^{K'}$) producing coccolithophorids are more abundant and thus more indicative of the climate signal of the low productive stratified season in this particular region. This hypothesis agrees with a recent core-top compilation of $U_{37}^{K'}$ derived SSTs indicating a warm bias in the estimated temperature within the Peruvian upwelling system [Prahl et al., 2009]. Consequently, accounting for seasonality in the interpretation of multi-proxy records from the EEP reveals that the amplitude of the seasonal SST cycle has increased over the Holocene, which agrees with precession-induced insolation changes (Figure 1) and the climate model results (Figure 6).

4. Implications of seasonal signals in paleo proxy records

Seasonal signals in paleo climate records are crucial for the interpretation of past climate evolution. For example, orbital forcing at the same latitude can either be positive or negative, depending on the season, which implies that phytoplankton organisms formed during spring, summer or fall blooms may exhibit contrasting climate trends (Figure 1a, d). Apart from this, temperature anomalies can also be transported latitudinally by advection. Both effects can explain the co-existence of strong positive and negative

Holocene SST trends even from the same proxy ($U_{37}^{K'}$) for example at 40^oN, where the annual mean insolation forcing is neutral (Figure 1b). Due to non-linear cloud feedbacks the insolation anomaly reaching the sea surface can be distinctly different, and sometimes even opposite in sign, from the insolation anomaly at the top of the atmosphere (Figure 1a-b). Therefore, a direct link between reconstructed temperature trends and insolation anomalies at the top of the atmosphere may be misleading.

An outstanding result of the data compilation by Leduc et al. [2010] is the general tendency of Mg/Ca records showing overall smoother climate trends than $U_{37}^{K'}$. This suggests that Mg/Ca records probably show results integrated over wider time and/or depth windows, which needs to be further investigated in future work. Species specific differences within the Mg/Ca data may also play a role for non-uniform trends. However, the diverging temperature trends from two locations in the North Atlantic [Leduc et al., 2010] are obtained from the same species (*G.bulloides*) and can therefore not unambiguously be explained by our model results.

For the calibration of core top proxy indices against modern SSTs seasonal effects may need to be taken into account. Particularly at high northern latitudes the SI (Figure 3) suggests a strong deviation of the climate signal in phytoplankton proxies from the annual mean toward higher temperatures. Similarly, in the tropics the application of annual mean SSTs may overestimate the temperatures registered by the proxies. Consequently, the temperatures used for proxy calibration may need to be revised toward lower values at the warm end, and toward higher values at the cold end, which suggests that a calibration curve as found in Prahl and Wakeham [1987] could result in a less steep slope

of temperatures increasing with $U_{37}^{K'}$, which would have implications for the temperature sensitivity of the $U_{37}^{K'}$-index. Therefore, we suggest that laboratory studies should focus on $U_{37}^{K'}$ calibrations in the temperature ranges where also a sigmoidal calibration curve is more or less linear, which means around 24^{o}C and 10^{o}C [Conte et al., 2006; Sonzogni et al., 1997; Sikes et al., 1997; Müller et al., 1998; Prahl and Wakeham, 1987].

Although seasonal subsampling can distinctly improve the agreement between model results and proxy data, there is still a general tendency of our model results to yield more positive temperature trends (positive intercepts of the regression line, see Figure 8 and Table 3), while at the same time it underestimates the reconstructed Holocene SST trends. The latter is very similar to results from other climate models [Brovkin et al., 2008; Voss and Mikolajewicz, 2001; Lorenz and Lohmann, 2004; Lorenz et al., 2006]. For $U_{37}^{K'}$ the slope of the regression line of the respective best filter yields a slope on the order of 0.24, which is considerably better than the slope for the annual mean values (0.07), but still far away from one, which would be expected for an ideal match. The regression coefficient, however, improves from R^2=0.10 to R^2=0.62 due to the seasonal subsampling. For Mg/Ca the slope of the regression line for the respective best filters is as good as for $U_{37}^{K'}$ (0.25), but the regression coefficient is still very low (R^2=0.17). Interestingly, for both proxies the filters T-MAX yield highest correlations (R^2=0.69 and R^2=0.78) among the individual filters and for the Mg/Ca data the regression slope is almost 1 (0.97). It remains an open question why climate models systematically underestimate climate trends. We suggest that one potential candidate is overly strong vertical mixing either in the atmosphere or in the ocean (or both) that would dampen the climate signal evolving at

the sea surface. A potential slight overestimate of the reconstructed trends, e.g. resulting from a too steep regression slope due to the neglect of seasonal SSTs in the calibration curve, is unlikely to have a sufficiently strong effect on SST trends. The neglect of other climate forcing mechanisms such as greenhouse gases and ice sheets is also unlikely. The radiative forcing of CO_2, which was increasing by 20 ppm over the Holocene [Indermühle et al., 1999] and of CH_4 which was around 750 ppb in the early and late Holocene with a minimum of 600 ppb between 5-6 Kyrs BP, is probably of minor importance compared to the effects of orbital forcing, considering temperature changes of a similar magnitude resulting from a doubling of CO_2 [Meehl et al., 2007]. A larger than present ice sheet over North America in the early Holocene has probably cooled the climate over the Northwest Atlantic Ocean [Renssen et al., 2009]. The neglect of this effect in a PMIP-type study should thus result in an underestimation of the warming trend in this area. In fact, the SST data show a very strong Holocene cooling in the western North Atlantic reaching a maximum reduction by -7.7 ^{o}C, which is the opposite from what would be expected from relaxation of the ice sheet impact, and our model even underestimates this cooling. It is therefore unlikely that the neglect of a larger than present ice sheet in the early Holocene has affected our model-data comparison.

Based on our findings we argue that in the North Atlantic a summer cooling trend shown by $U_{37}^{K'}$ and a winter warming given by Mg/Ca can be reconciled by a reduction in the amplitude of the seasonal SST cycle over the Holocene, which is in agreement with insolation forcing (Figure 1). This may have further implications for the global carbon cycle, as the North Atlantic is the main region for uptake and southward transport of CO_2

from the atmosphere [Mikaloff-Fletcher et al., 2007] and the highest air-sea CO_2 fluxes are taking place during the winter season [Takahashi et al., 2009]. Consequently, we hypothesize that seasonality plays a role in the air-sea carbon flux, so that in contrast to findings from Brovkin et al. [2008] a slight early Holocene winter cooling followed by a more pronounced late Holocene winter warming in the formation areas of North Atlantic Deep Water, as simulated by our climate model (not shown), may be qualitatively reconciled with the Holocene evolution of atmospheric CO_2 concentrations detected from ice core records [Indermühle et al., 1999], which needs to be tested in future work.

5. Summary and Conclusions

In a careful combination of multi-proxy data with climate model results and modern satellite data, we have illustrated how the different sensitivities of atmosphere, ocean, and marine biology to changes in external climate forcing result in a strongly non-linear modulation of the climate signal that is ultimately shaping proxy records (Figure 1). This confirms the hypothesis that the same external forcing may have a different impact on various proxy organisms, resulting in apparently contrasting climate trends. The a priori knowledge on the seasonal relationship between sea surface temperature (SST) and net primary production (NPP), which was obtained from modern satellite data and used as an independent link, enabled us to bring model and proxy results closer together. Nevertheless, we find that our (and probably other) climate model(s) systematically underestimate climate trends [Brovkin et al., 2008; Voss and Mikolajewicz, 2001; Lorenz and Lohmann, 2004; Lorenz et al., 2006], which needs further investigation. Our findings give a more robust view on which climate signals are probably contained in the two most commonly

used proxies for SST ($U_{37}^{K'}$ and Mg/Ca), which is crucial for model-data comparisons aiming at evaluating the ability of models to simulate past climates [Braconnot et al., 2007]. Our results imply that a careful application of multi-proxy approaches opens new perspectives, such as to go beyond the reconstruction of annual average climate trends, and to resolve the evolution of the seasonal cycle in the past. Paleo climate reconstructions can therefore be refined including seasonal climate variability, which provides better hypotheses against which climate models can be tested. We believe that the detected latitudinal preference of a phytoplankton proxy for recording the warm (cold) season in high (low) latitudes is a robust feature that may also be valid for different climate states such as the last glacial maximum [MARGO, 2009].

Acknowledgments. We thank M. Behrenfeld for valuable discussions and for providing the satellite data of marine net primary production (NPP). We also thank C. Charles and an anonymous reviewer who provided very constructive comments that helped to improve the manuscript. This work presents results from a collaboration between the DFG-supported Cluster of Excellence The Future Ocean (EXC 80/1), INTERDYNAMICS and SFB754.

References

Aumont, O., E. Maier-Reimer, S. Blain, and P. Monfray (2003), An ecosystem model of the global ocean including Fe, Si, P colimitations, *Global Biogeochemical Cycles*, *17(2)*(1060), doi:10.1029/2001GB001745.

Behrenfeld, M. J., R. T. O'Malley, D. A. Siegel, C. R. McClain, J. L. Sarmiento, G. C. Feldman, A. J. Milligan, P. G. Falkowski, R. M. Letelier, and E. S. Boss (2006),

Climate-driven trends in contemporary ocean productivity, *Nature*, *444*, 752–755.

Bijma, J., M. Altabet, M. Conte, H. Kinkel, G. J. M. Versteegh, J. K. Volkman, S. G. Wakeham, and P. P. Weaver (2001), Primary signal: Ecological and environmental factors – Report from Working Group 2, *Geochemistry Geophysics Geosystems*, *2*, doi: 2000GC000051.

Blain, S., B. Quéguiner, L. Armand, S. Belviso, B. Bombled, L. Bopp, A. Bowie, C. Brunet, C. Brusaard, F. Carlotti, U. Christaki, A. Corbiere, I. Durand, F. Ebersbach, J. L. Fuda, N. Garcia, L. Gerringa, B. Griffiths, C. Guigue, C. Guillerm, S. Jacquet, C. Jeandel, P. Laan, D. Lefèvre, C. Lo Monaco, A. Malits, J. Mosseri, I. Obernosterer, Y.-H. Park, M. Picheral, P. Pondaven, T. Remenyi, V. Sandroni, G. Sarthou, N. Savoye, L. Scouarnec, M. Souhaut, D. Thuiller, K. Timmermans, T. Trull, J. Uitz, P. vanBeek, M. Veldhuis, D. Vincent, E. Viollier, L. Vong, and T. Wagener (2007), Effect of natural iron fertilization on carbon sequestration in the Southern Ocean, *Nature*, *446*, 1070–1074, doi:10.1038/nature05700.

Boyd, P. W., and T. W. Trull (2007), Understanding the export of biogenic particles in oceanic waters: Is there consensus?, *Progress in Oceanography*, *72*, 276–312, doi: 10.1016/j.pocean.2006.10.007.

Braconnot, P., B. Otto-Bliesner, S. Harrison, S. Joussaume, J. Y. Peterschmitt, A. Abe-Ouchi, M. Crucifix, E. Driesschaert, T. Fichefet, C. D. Hewitt, M. Kageyama, A. Kitoh, A. Lainé, M. F. Loutre, O. Marti, U. Merkel, G. Ramstein, P. Valdes, L. Weber, Y. Yu, and Y. Zhao (2007), Results of PMIP2 coupled simulations of the Mid-Holocene and Last Glacial Maximum - Part 1: experiments and large-scale features, *Climate of*

the Past, *3*(2), 261–277.

Braconnot, P., C. Marzin, L. Grégoire, E. Mosquet, and O. Marti (2008), Monsoon response to changes in Earth's orbital parameters: comparisons between simulations of the Eemian and of the Holocene, *Climate of the Past*, *3*, 281–294.

Brovkin, V., J.-H. Kim, M. Hofmann, and R. Schneider (2008), A lowering effect of reconstructed Holocene changes in sea surface temperatures on the atmospheric CO_2 concentration, *Global Biogeochemical Cycles*, *22*(GB1016), doi: 10.1029/2006GB002885.

Conkright, M. E., R. A. Locarnini, H. E. Garcia, T. D. O'Brien, T. P. Boyer, C. Stephens, and J. I. Antonov (2002), World ocean atlas 2001: Objective analyses, data statistics, and figures, *CD-ROM documentation*, NOAA, Silver Spring.

Conte, M. H., M. A. Sicre, C. Rühlemann, J. C. Weber, S. Schulte, D. Schulz-Bull, and T. Blanz (2006), Global temperature calibration of the alkenone unsaturation index ($U_{37}^{K'}$) in surface waters and comparison with surface sediments, *Geochemistry Geophysics Geosystems*, *7*(2), doi:10.1029/2006GC001054.

Fichefet, T., and M. A. Morales Maqueda (1997), Sensitivity of a global sea ice model to the treatment of ice thermodynamics and dynamics, *Journal of Geophysical research*, *102*, 12,609–12,646.

Fraile, I., M. Schulz, S. Mulitza, U. Merkel, M. Prange, and A. Paul (2009a), Modeling the seasonal distribution of planktonic foraminifera during the Last Glacial Maximum, *Paleoceanography*, *24*(PA2216), doi:10.1029/2008PA001686.

Fraile, I., S. Mulitza, and M. Schulz (2009b), Modeling planktonic foraminiferal seasonality: Implications for sea-surface temperature reconstructions, *Marine Micropaleontology*, *72*, 1–9.

Gehlen, M., L. Bopp, N. Emprin, O. Aumont, C. Heinze, and O. Ragueneau (2006), Reconciling surface ocean productivity, export fluxes and sediment composition in a global biogeochemical ocean model, *Biogeosciences*, *3*, 521–537.

Hutchins, D. A., and K. W. Bruland (1998), Iron-limited diatom growth and Si:N uptake ratios in a coastal upwelling regime, *Nature*, *393*, 561–564.

Huybers, P., and G. Denton (2008), Antarctic temperature at orbital timescales controlled by local summer duration, *Nature Geoscience*, *1*, 787–792, doi: 10.1038/NGEO311.

Huybers, P., and C. Wunsch (2003), Rectification and precession signals in the climate system, *Geophysical Research Letters*, *30*(19), doi:10.1029/2003GL017875.

Indermühle, A., T. F. Stocker, F. Joos, H. Fischer, H. J. Smith, M. Wahlen, B. Deck, D. Mastroianni, T. Tschumi, T. Blunier, R. Meyer, and B. Stauffer (1999), Holocene carbon-cycle dynamics based on CO_2 trapped in ice at Taylor Dome, Antarctica, *Nature*, *398*, 121–126.

Joussaume, S., and K. E. Taylor (1995), Status of the Paleoclimate Modeling Intercomparison Project (PMIP), in *Proceedings of the first international AMIP scientific conference*, pp. 425–430, WCRP-92, Monterey, USA.

Kim, J. H., N. Rimbu, S. J. Lorenz, G. Lohmann, S. I. Nam, S. Schoutene, C. Rühlemann, and R. R. Schneider (2004), North Pacific and North Atlantic sea-

surface temperature variability during the Holocene, *Quaternary Science Reviews*, *23*, 2141–2154.

Laepple, T., and G. Lohmann (2009), The seasonal cycle as template for climate variability on astronomical time scales, *Paleoceanography*, doi:10.1029/2008PA001674.

Laws, E. A., P. G. Falkowski, W. O. Smith, and H. Ducklow (2000), Temperature effects on export production in the open ocean, *Global Biogeochemical Cycles*, *14*(4), 1231–1246.

Leduc, G., R. Schneider, J. H. Kim, and G. Lohmann (2010), Holocene and Eemian sea surface temperature trends as revealed by alkenone and Mg/Ca Paleothermometry, *Quaternary Science Reviews*, (29), 989–1004.

LeGrande, A. N., and G. A. Schmidt (2009), Sources of holocene variability of oxygen isotopes in paleoclimate archives, *Climate of the Past*, *5*(5), 441–455.

Lorenz, S., and G. Lohmann (2004), Acceleration technique for Milankovitch type forcing in a coupled atmosphere-ocean circulation model: method and application for the Holocene, *Climate Dynamics*, *23*, 727–743.

Lorenz, S., J. H. Kim, N. Rimbu, R. R. Schneider, and G. Lohmann (2006), Orbitally driven insolation forcing on Holocene climate trends: Evidence from alkenone data and climate modeling, *Paleooceanogorahy*, *21*(PA1002), doi:10.1029/2005PA001152.

Madec, G. (2008), NEMO ocean engine. Notes du Pole de Modélisation 27, *Tech. rep.*, Institut Pierre Simon Laplace, Paris.

Mann, M. E., G. A. Schmidt, S. K. Miller, and A. N. LeGrande (2009), Potential biases in inferring Holocene temperature trends from long-term borehole information,

Geophysical Research Letters, *36*, doi:10.1029/2008GL036354.

MARGO (2009), Constraints on the magnitude and patterns of ocean cooling at the Last glaical Maximum, *Nature Geoscience*, *2*, 1–6, doi:10.1038/NGEO411.

Martin, J. H., S. E. Fitzwater, and R. M. Gordon (1990), Iron deficiency limits phytoplanton growth in antarctic waters, *Global Biogeochemical Cycles*, *4*(1), 5–12.

Meehl, G. A., T. F. Stocker, W. D. Collins, P. Friedlingstein, A. T. Gaye, J. M. Gregory, A. Kitoh, R. Knutti, M. Murhpy, A. Noda, S. C. B. Raper, I. G. Watterson, A. J. Weaver, and Z. C. Zhao (2007), Global Climate Projections, in *Climate Change 2007: The Physical Science Basis. Contribution of Working Group I to the Fourth Assessment Report of the Intergovernmental Panel on Climate Change [Solomon, S., D. Quin, M. Manning, Z. Chen, M. Marquis, K.B. Averyt, M. Tignor and H.L. Miller (eds.)]*, Cambridge University Press, Cambridge, United Kingdom and New York, NY, USA.

Mikaloff-Fletcher, S. E., N. Gruber, A. R. Jacoboson, M. Gloor, S. C. Doney, S. Dutkiewicz, M. Gerber, M. Follows, F. Joos, K. Lindsay, D. Menemenlis, A. Mouchet, S. A. Müller, and J. L. Sarmiento (2007), Inverse estimates of the oceanic sources and sinks of natural CO_2 and the implied oceanic carbon transport, *Global Biogeochemical Cycles*, *21*, doi:0.1029/2006GB002751.

Mix, A., W. F. Ruddiman, and A. McIntyre (1986), Late Quaternary Paloceanography of the tropical Atlantic, 2: the seasonal cycle of sea surface temperatures, 0-20,000 years B.P., *Paleoceanography*, *1*(3), 339–353.

Müller, P. J., G. Kirst, G. Ruhland, I. von Storch, and A. Rosell-Melé (1998), Calibration of the alkenone paleotemperature index $U^{k'}_{37}$ based on core-tops from the eastern South

Atlantic and the global ocean (60^{o}N-60^{o}S), *Geochimica et Cosmochimica Acta*, *62*, 1757–1772.

Nürnberg, D., J. Bijma, and C. Hemleben (1996), Assessing the reliability of magnesium in foraminiferal calcite as a proxy for water mass temperatures, *Geochimica et Cosmochimica Acta*, *60*, 803–814.

Oppo, D. W., Y. Rosenthal, and B. K. Linsley (2009), 2,000-year-long temperature and hydrology reconstructions from the IndoPacific warm pool, *Nature*, *460*, 1113–1116, doi:10.1038/nature08233.

Park, W., and M. Latif (2008), Multidecadal and multicentennial variability of the meridional overturning circulation, *Geophysical Research Letters*, doi: 10.1029/2008GL035779.

Park, W., N. Keenlyside, M. Latif, A. Stroeh, R. Redler, E. Roeckner, and G. Madec (2009), Tropical Pacific Climate and Its Response to Global Warming in the Kiel Climate Model, *Journal of Climate*, pp. 71–92.

Prahl, F. G., and S. G. Wakeham (1987), Calibration of unsaturation patterns in long-chain ketone compositions for paleotemperature assessment, *Nature*, *330*, 367–369.

Prahl, F. G., J.-F. Rontani, N. Zabeti, S. E. Walinsky, and M. A. Sparrow (2009), Systematic pattern in $U^{k'}_{37}$-Temperature residuals for surface sediments from high latitude and other oceanographic settings, *Geochimica et Cosmochimica Acta*, doi: 10.1016/j.gca.2009.09.027.

Regenberg, M., S. Steph, D. Nürnberg, R. Tiedemann, and D. Garbe-Schönberg (2009), Calibrating Mg/Ca ratios of multiple planktonic foraminiferal species with δ^{18}O-

calcification temperatures: paleothermometry for the upper water column, *Earth and Planetary Science Letters*, *278*, 324–336.

Renssen, H., H. Seppä, O. Heiri, D. M. Roche, H. Goosse, and T. Fichefet (2009), The spatial and temporal complexity of the Holocene thermal maximum, *Nature Geoscience*, *2*, 411–414, doi:10.1038/NGEO513.

Reynolds, R. W., T. M. Smith, C. Liu, D. B. Chelton, K. S. Caesy, and M. G. Schlax (2007), Daily high-resolution blended analyses for sea surface temperature, *Journal of Climate*, *20*, 5473–5496.

Roeckner, E., R. Brokopf, M. Esch, M. Giorgetta, S. Hagemann, L. Kornblueh, E. Manzini, U. Schlese, and U. Schulzweida (2003), The atmospheric general circulation model ECHAM5. Part I: Model description, Rep. 349, *Tech. rep.*, Max Planck Institut für Meteorologie, Hamburg, Germany.

Schneider, B., L. Bopp, M. Gehlen, J. Segschneider, T. L. Frölicher, P. Cadule, P. Friedlingstein, S. C. Doney, M. Behrenfeld, and F. Joos (2008), Climate-induced interannual variability of marine primary and export production in three global coupled climate carbon cycle models, *Biogeosciences*, *5*, 597–614.

Sikes, E. L., J. K. Volkman, L. G. Robertson, and J.-J. Pichon (1997), Alkenones and alkenes in surface waters and sediments of the Southern Ocean: Implications for paleotemperature estimation in polar regions, *Geochimica et Cosmochimica Acta*, *61*(7), 1495–1505.

Sonzogni, C., E. Bard, F. Rostek, R. Lafont, A. Rosell-Melé, and G. Eglinton (1997), Core-top calibration of the alkenone index vs sea surface temperature in the Indian

Ocean, *Deep-Sea Research II*, *44*(6-7), 1445–1460.

Takahashi, T., S. C. Sutherland, R. Wanninkhof, C. Sweeney, R. A. Feely, D. W. Chipman, B. Hales, G. Friederich, F. Chavez, C. Sabine, A. Watson, D. C. Bakker, U. Schuster, N. Metzl, H. Yoshikawa-Inoue, M. Ishii, T. Midorikawa, Y. Nojiri, A. Körtzinger, T. Steinhoff, M. Hoppema, J. Olafsson, T. S. Arnarson, B. Tilbrook, T. Johannessen, A. Olsen, R. Bellerby, C. Wong, B. Delille, N. Bates, and H. J. de Baar (2009), Climatological mean and decadal change in surface ocean pCO_2, and net sea-air CO_2 flux over the global oceans, *Deep-Sea Research II*, *56*(8-10), 554–577, doi:10.1016/j.dsr2.2008.12.009.

Ternois, Y., M.-A. Sicre, A. Boireau, L. Beaufort, J.-C. Miquel, and C. Jeandel (1998), Hydrocarbons, sterols and alkenones in sinking particles in the Indian Ocean sector of the Southern Ocean, *Organic Geochemistry*, *28*(7-8), 489–501.

Thunell, R. C., W. B. Curry, and S. Honjo (1983), Seasonal variation in the flux of planktonic foraminifera: time series sediment trap results from the Panama Basin, *Earth and Planetery Science Letters*, *64*, 44–55.

Valcke, S. (2003), OASIS3 user guide, PRISM Tech. Rep. 3 , *Tech. rep.*, Partnership for Research Intrastructures in Earth System Modeling, Toulouse, France.

Voss, R., and U. Mikolajewicz (2001), The climate of 6000 years BP in near-equilibrium simulations witha coupled AOGCM, *Geophysical Research Letters*, *28*(11), 2213–2216.

Figure 1. Sensitivity of the climate system to changes in orbital forcing. (a) The spatio-temporal redistribution of solar insolation over the Holocene (0K minus 9.5K) at the top of the atmosphere (shaded) is highlighting changes in the seasonal cycle caused by precessional effects. Contour lines of the respective anomaly which is reaching the sea surface indicate the feedback of changing cloud properties. (b) The latitudinal distribution of the annual mean insolation anomaly at the top of the atmosphere (black line) is caused by decreasing obliquity. The red line shows the strongly modulated signal (due to non-linear cloud feedbacks) arriving at the sea surface. Symbols mark reconstructed temperature changes at the respective latitudes, based on $U_{37}^{K'}$ (dots) and Mg/Ca (triangles). (c) The seasonal zonal mean mixed layer depth shows time periods when the surface ocean is well stratified (red) and thus more susceptible to insolation forcing [Laepple and Lohmann, 2009]. (d) The relative net primary production (monthly zonal mean divided by annual zonal mean) shows the seasonal variability of plankton productivity, thus the sensitivity of marine biology to insolation forcing [Behrenfeld et al., 2006].

Figure 2. Map of the locations of marine sediment cores from which paleo SST data is available [Leduc et al., 2010] (black: $U_{37}^{K'}$; red: Mg/Ca). The core locations are numbered according to the data Tables 1 and 2.

Figure 3. (a) Modern distribution of the seasonality index (SI; see methods), highlighting areas where SST and NPP are strongly correlated, i.e. where NPP is rising either with increasing (red; positive correlation) or with decreasing (blue; negative correlation) SST. Grey shaded areas indicate a modern seasonal SST amplitude below 2^oC, which probably would not be captured by proxy records. (b) Zonal average SI. (c) Trends of annual mean SST (T-ANN) over the full Holocene (0K minus 9.5K) as simulated by the model (shaded), superimposed with reconstructions from $U_{37}^{K'}$ (dots) and Mg/Ca (triangles). (d) Same as in (c) but for SST trends weighted by the SI (SI-WEIGHT).

Figure 4. Comparison of different filters for Holocene SST trends. Green colors indicate where the respective filtered trend (a; T-MAX, b; T-MIN, c; SI-WEIGHT; see explanations in the text) is getting closer to the reconstructed proxy value for $U_{37}^{K'}$ (dots) and Mg/Ca (triangles) than the annual mean (T-ANN). Red colors show where the annual mean from the model yields a better or equal result. The numbers show in how many cases the respective filtered trend is getting better (+) or is equal or worse (-) than the annual mean.

Figure 5. Maps showing the filter yielding the best match with the proxy data at the respective locations for (a) $U_{37}^{K'}$ and (b) Mg/Ca ratios. The larger the symbol the greater the improvement, i.e. the lower the relative error (reduction of mismatch; C [%]) of the filtered result relative to the annual mean (see explanations in the text).

Figure 6. Modeled and reconstructed Holocene sea surface temperature (SST) trends in the Eastern Equatorial Pacific. Model results (shaded) are superimposed with reconstructions by $U_{37}^{K'}$ (dots) and Mg/Ca (triangles). Arrows show the modeled anomalies in surface currents and numbers indicate the insolation anomalies arriving at the sea surface in the respective hemispheres displayed in the Figure. All trends are separated into early Holocene (a, e, i; first column), late Holocene (b, f, j; second column), and full Holocene trends (c, g, k; third column). The model results are furthermore split up into SST trends for the annual mean (a-c; top row), boreal summer (d-f; JAS; middle row), and boreal winter (g-i; JFM; bottom row) SST trends. For reference, the right column shows the absolute values of SST, surface currents and insolation for the annual mean (d), the boreal summer upwelling season (h) and the boreal winter stratified season (l) from the preindustrial (H0K) simulation.

Figure 7. Modeled and observed seasonal cycle of SST and NPP in the Eastern Equatorial Pacific (100^oW-80^oW, Eq-5^oS). Dashed lines are from observations (red: SST [Reynolds et al., 2007]; black: NPP [Behrenfeld et al., 2006]), full lines show results from a preindustrial simulation of the IPSL-PISCES marine biogeochemical model [Gehlen et al., 2006]. The blue line indicates the relative contribution of diatoms to total phytoplankton biomass, dominating during the high productive season (JAS).

Figure 8. Regression of reconstructed versus modeled SST-Trends for $U_{37}^{K'}$ (a) and Mg/Ca (g). The modeled trends are shown for the annual mean values (T-ANN; open symbols) and the respective seasonally subsampled value that was yielding the best match with the data at each location (grey: T-ANN; green: SI-WEIGHT; red: T-MAX; blue: T-MIN). Regression lines are shown for the annual mean values (dashed line) and the trends based on the best filter (black line), the resulting statistics are given in Table 3.

Table 1. Reconstructed Holocene SST trends from $U_{37}^{K'}$ [Leduc et al., 2010] and corresponding model-derived SST trends (^{o}C) based on different filters at the respective core site (see Figure 2).

n	lat(^{o}N)	lon(^{o}E)	$U_{37}^{K'}$	T-ANN	SI-WEIGHT	T-MAX	T-MIN
1	67.0	-18.0	-2.3	-0.16	-0.36	-0.54	0.00
2	58.8	-26.0	-0.9	0.12	-0.24	-0.50	0.28
3	57.7	7.1	-1.9	0.14	-0.04	-0.46	0.20
4	48.9	-126.9	-1.4	0.22	-0.35	-0.84	0.67
5	48.2	151.3	2.1	-0.58	-1.44	-1.96	0.07
6	44.5	145.0	1.5	-0.06	-0.82	-1.83	0.78
7	43.9	-62.8	-6.3	-0.19	-0.80	-1.12	0.33
8	43.5	-54.9	-7.7	-0.40	-0.91	-1.41	0.20
9	41.7	-124.9	-0.6	0.16	-0.37	-0.91	0.64
10	37.9	-10.2	-0.7	0.50	0.40	-0.17	0.72
11	37.8	-10.2	0.0	0.50	0.40	-0.17	0.72
12	37.8	-10.2	-0.6	0.50	0.40	-0.17	0.72
13	36.9	-74.6	-3.5	0.34	0.53	-0.55	0.68
14	34.5	-121.1	1.7	0.08	-0.66	-1.07	0.71
15	32.7	138.5	0.1	1.02	1.27	0.64	1.41
16	31.1	138.7	0.9	1.04	1.24	0.81	1.37
17	23.6	64.2	0.8	0.66	0.83	-0.49	1.03
18	23.0	-109.5	0.1	0.32	0.73	-0.48	0.93
19	20.8	-18.6	0.9	0.43	0.31	0.23	0.57
20	20.2	-18.5	0.7	0.43	0.31	0.23	0.57
21	20.1	117.4	1.7	0.79	1.04	0.17	1.29
22	20.0	90.0	0.6	1.12	0.59	0.37	2.14
23	19.0	-20.2	-0.3	0.74	0.73	0.73	0.83
24	18.0	111.5	1.5	0.69	0.81	0.05	1.09
25	14.3	57.3	0.7	0.74	0.34	0.34	1.04
26	12.0	-61.3	1.3	0.15	-0.41	-0.73	0.62
27	11.1	52.0	0.4	0.71	0.50	0.80	1.04
28	10.7	-65.2	0.0	-0.02	0.43	-1.01	0.57
29	10.5	75.2	0.1	0.54	-0.07	1.26	-0.10
30	8.0	-84.1	1.6	0.18	-0.05	-0.73	0.80
31	4.8	-78.0	2.1	0.24	1.01	0.09	-0.46
32	3.2	50.4	0.2	0.63	0.37	0.92	1.05
33	2.5	9.4	1.8	1.01	0.72	0.74	1.73
34	-0.5	-82.7	1.2	-0.34	-0.73	0.42	-1.58
35	-2.5	-84.7	0.5	-0.24	-0.70	0.53	-1.02
36	-3.4	-83.5	0.4	-0.23	-0.38	0.49	-0.95
37	-3.9	-36.3	0.4	0.82	0.50	1.30	0.51
38	-4.6	-35.9	0.2	0.82	0.51	1.48	0.51
39	-5.6	11.2	0.3	0.64	0.51	0.17	0.75
40	-6.5	103.8	1.2	0.85	0.95	0.66	1.16

Table 1. cont.

n	lat(^{o}N)	lon(^{o}E)	$U_{37}^{K'}$	T-ANN	SI-WEIGHT	T-MAX	T-MIN
41	-11.9	13.4	1.2	0.49	0.16	0.67	-0.05
42	-17.2	11.0	-0.3	0.31	0.20	0.80	-0.03
43	-20.4	36.3	0.6	0.61	0.34	1.18	0.29
44	-30.2	-72.0	-1.5	0.39	0.25	0.67	0.37
45	-32.8	-72.0	-0.3	0.39	0.27	0.68	0.40
46	-36.7	136.6	-1.0	0.41	0.46	0.94	0.06
47	-41.0	-74.5	-1.6	0.48	0.48	0.79	0.39
48	-43.4	167.9	-1.9	0.46	0.30	0.46	0.48
49	-45.5	179.5	-0.2	0.48	0.44	0.56	0.55
50	-45.5	174.9	-2.9	0.28	0.28	0.39	0.28
51	50.4	148.3	-0.1	-0.72	-1.67	-2.47	0.03
52	30.9	-10.3	-1.4	0.52	0.29	0.03	0.62
53	38.6	9.5	-3.0	0.47	0.22	0.21	0.69
54	21.4	-158.2	1.5	0.34	0.52	0.07	0.59

Table 2. Reconstructed Holocene SST trends from Mg/Ca ratios [Leduc et al., 2010], corresponding model-derived SST trends (^{o}C) based on different filters at the respective core site (Figure 2), and species used for the respective reconstruction.

n	lat(^{o}N)	lon(^{o}E)	Mg/Ca	T-ANN	SI-WEIGHT	T-MAX	T-MIN	Species
1	2.50	9.40	-1.60	1.01	0.72	0.74	1.73	*G. ruber (pink)*
2	2.50	9.40	-0.20	1.01	0.72	0.74	1.73	*G. ruber (pink)*
3	-4.60	-36.60	-0.20	0.79	0.47	1.40	0.45	*G. ruber (white)*
4	-1.20	-89.70	0.60	0.05	-0.52	1.04	-0.81	*G. sacculifer*
5	10.70	-65.90	-0.20	-0.02	0.43	-1.01	0.57	*G. ruber (white)*
6	6.30	126.10	-0.80	0.25	0.11	-0.45	0.70	*G. ruber (white)*
7	-5.00	133.40	-0.30	0.24	-0.05	0.28	-0.38	*G. ruber (white)*
8	-10.60	125.40	-0.80	0.35	0.11	0.14	0.23	*G. ruber (white)*
9	7.90	-83.60	0.20	0.20	-0.06	-0.70	0.86	*G. ruber (white)*
10	-25.50	13.30	-0.90	0.78	0.75	1.09	0.60	*G. bulloides*
11	-4.70	117.90	0.20	0.45	0.98	-0.04	0.90	*G. ruber*
12	19.00	-20.20	0.10	0.74	0.73	0.73	0.83	*G. ruber + G. bulloides*
13	61.00	-25.00	0.70	0.08	-0.27	-0.52	0.30	*N. Pachyderma (d)*
14	27.80	127.00	0.10	0.96	1.22	0.83	1.36	*G. ruber*
15	0.00	-86.40	-0.70	-0.20	-0.76	0.58	-1.21	*G. ruber*
16	57.40	-27.90	2.40	0.16	-0.22	-0.47	0.31	*G. bulloides*
17	29.00	-87.10	-1.30	0.17	0.50	-0.70	0.62	*G. ruber*
18	0.50	-92.40	-0.40	0.01	-0.64	0.80	-0.86	*G. ruber*
19	43.50	-54.90	-0.80	-0.40	-0.91	-1.41	0.20	*G. bulloides*
20	-9.60	118.30	1.60	0.36	0.18	0.12	0.12	*G. ruber*
21	2.30	-91.00	0.10	0.07	-0.40	-0.02	0.63	*G. ruber*
22	-45.50	174.90	-0.90	0.28	0.28	0.39	0.28	*G. bulloides*
23	-13.10	121.80	-0.70	0.32	0.15	0.00	0.14	*G. ruber*
24	62.10	-17.80	-0.90	-0.08	-0.47	-0.73	0.16	*G. bulloides*
25	6.60	113.40	-0.60	0.29	0.80	-0.47	1.09	*G. ruber s.s.*
26	37.8	-10.2	1.6	0.50	0.40	-0.17	0.73	*G. bulloides*

Table 3. Regression of observed versus modeled SST trends for the two paleo proxies $U_{37}^{K'}$ (top) and Mg/Ca (bottom) and the different SST trends from the model based on the annual mean (T-ANN), the best filter available (BEST) at the respective location, and the individual filters (T-MAX, T-MIN, SI-WEIGHT) when yielding best results (see also Figure 8).

$U_{37}^{K'}$	slope	intercep	R^2	n
T-ANN	0.07	0.40	0.10	54
BEST	0.24	0.36	0.62	54
T-MAX	0.22	0.22	0.69	20
T-MIN	0.26	0.42	0.33	17
SI-WEIGHT	0.22	0.38	0.40	12
$U_{37}^{K'}$	slope	intercep	R^2	n
T-ANN	-0.01	0.32	0.00	26
BEST	0.25	0.13	0.17	26
T-MAX	0.96	0.34	0.78	9
T-MIN	0.06	0.30	0.04	6
SI-WEIGHT	-0.38	-0.41	0.06	6

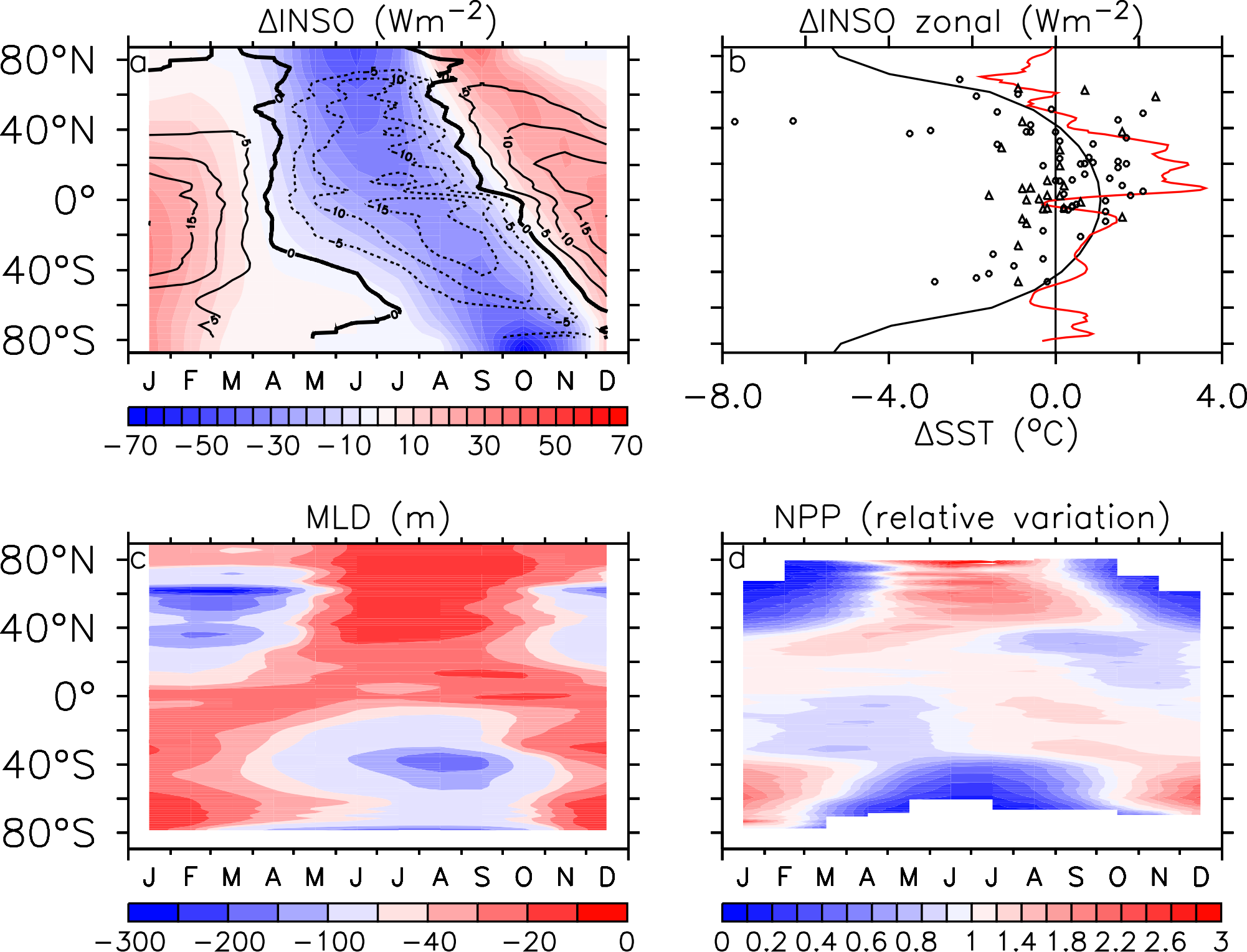
ΔINSO (Wm^{-2})
a
80°N
40°N
0°
40°S
80°S
J F M A M J J A S O N D
−70 −50 −30 −10 10 30 50 70
ΔINSO zonal (Wm^{-2})
b
−8.0 −4.0 0.0 4.0
ΔSST (°C)
MLD (m)
c
−300 −200 −100 −40 −20 0
NPP (relative variation)
d
0 0.2 0.4 0.6 0.8 1 1.4 1.8 2.2 2.6 3

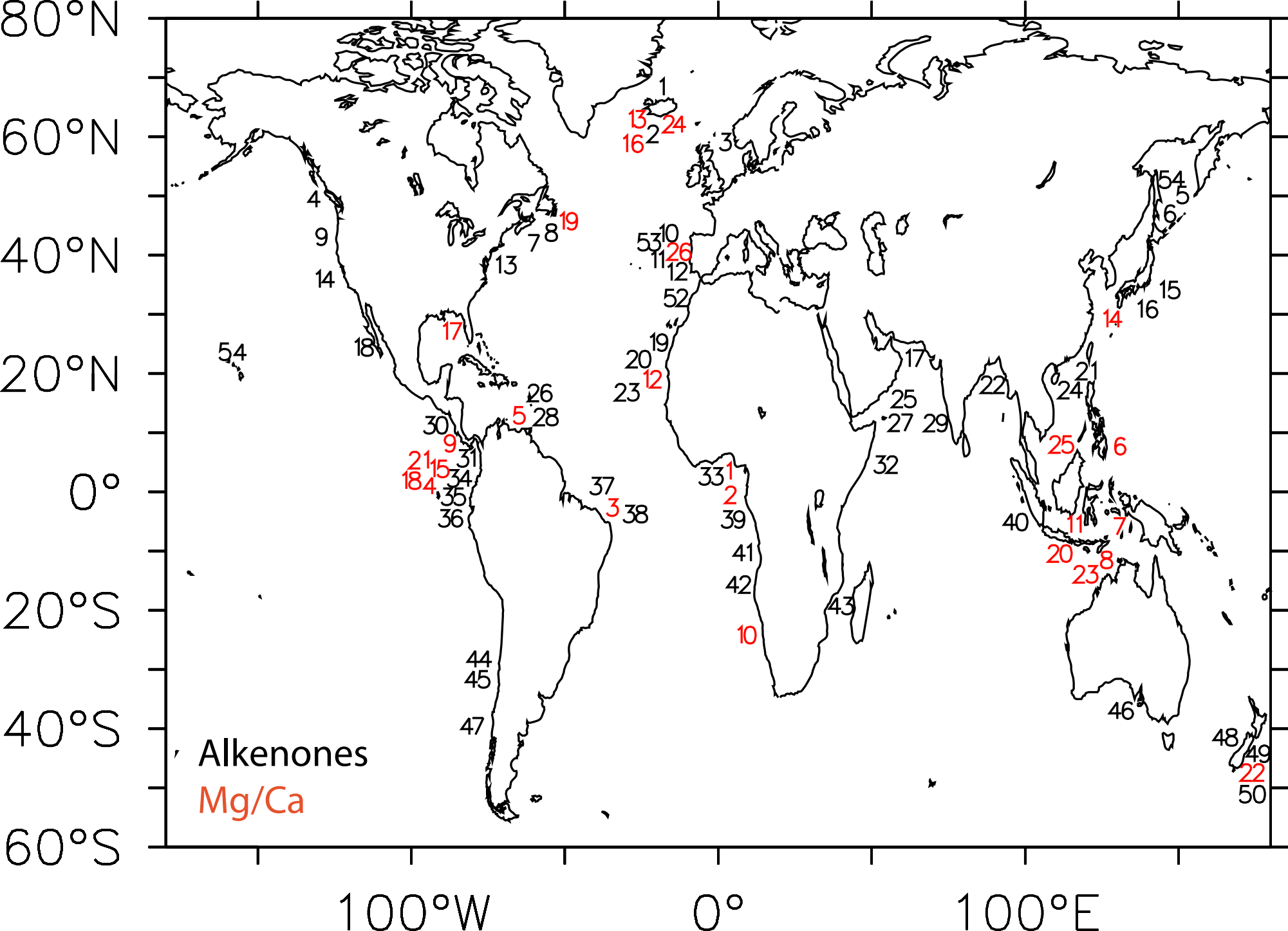
80°N
60°N
40°N
20°N
0°
20°S
40°S
60°S
100°W
0°
100°E
Alkenones
Mg/Ca

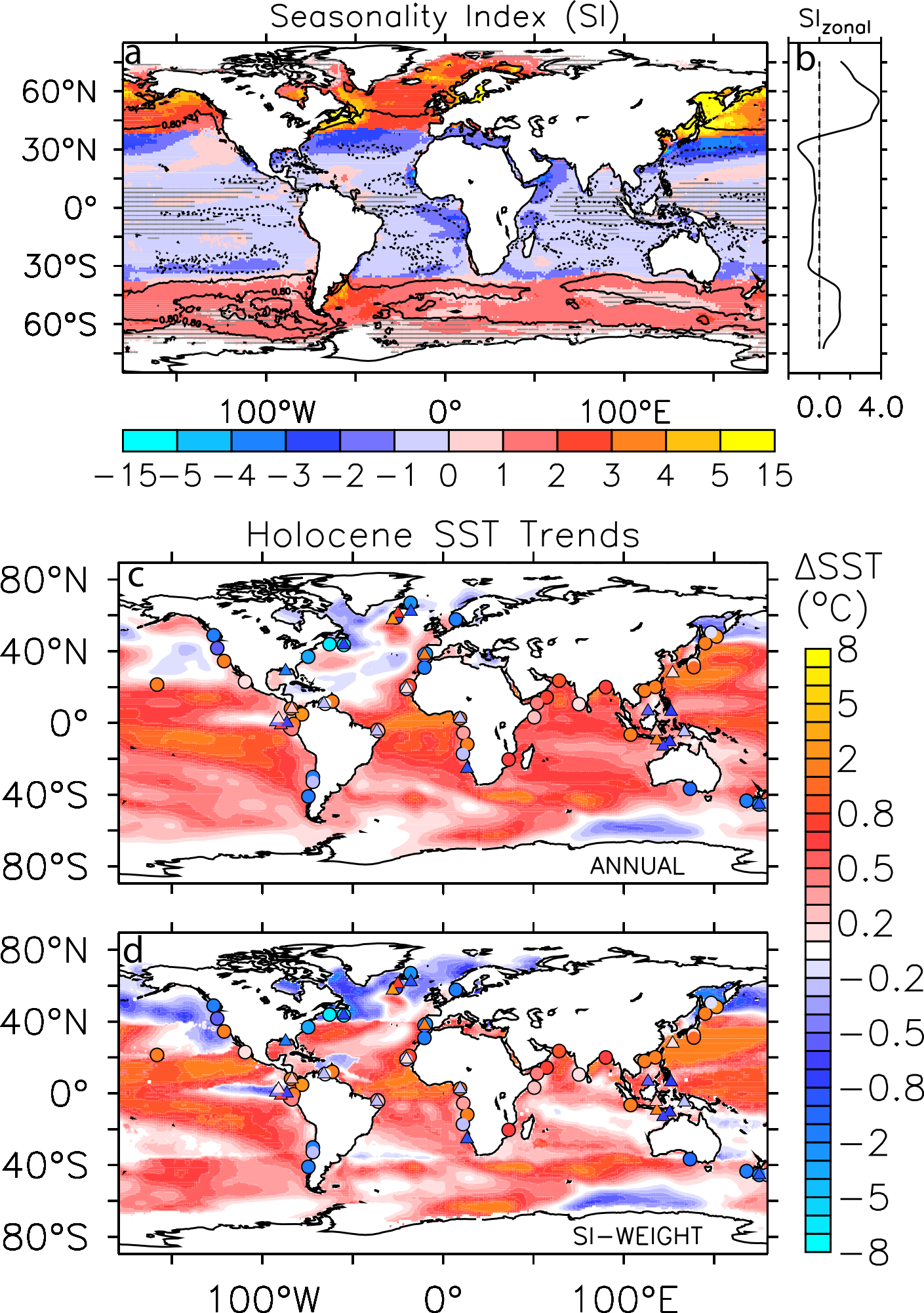
Seasonality Index (SI)
a
b
SI zonal
60°N
30°N
0°
30°S
60°S
0.80
100°W
0°
100°E
0.0 4.0
−15 −5 −4 −3 −2 −1 0 1 2 3 4 5 15
Holocene SST Trends
c
d
80°N
40°N
0°
40°S
80°S
ANNUAL
SI−WEIGHT
ΔSST
(°C)
8
5
2
0.8
0.5
0.2
−0.2
−0.5
−0.8
−2
−5
−8

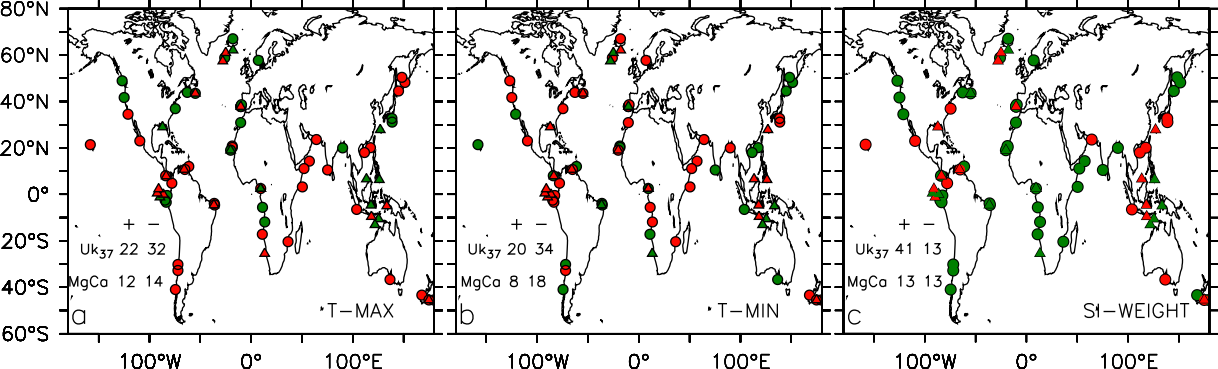
80°N
60°N
40°N
20°N
0°
20°S
40°S
60°S
100°W
0°
100°E
+ −
Uk37 22 32
MgCa 12 14
a
T−MAX
+ −
Uk37 20 34
MgCa 8 18
b
T−MIN
+ −
Uk37 41 13
MgCa 13 13
c
SI−WEIGHT

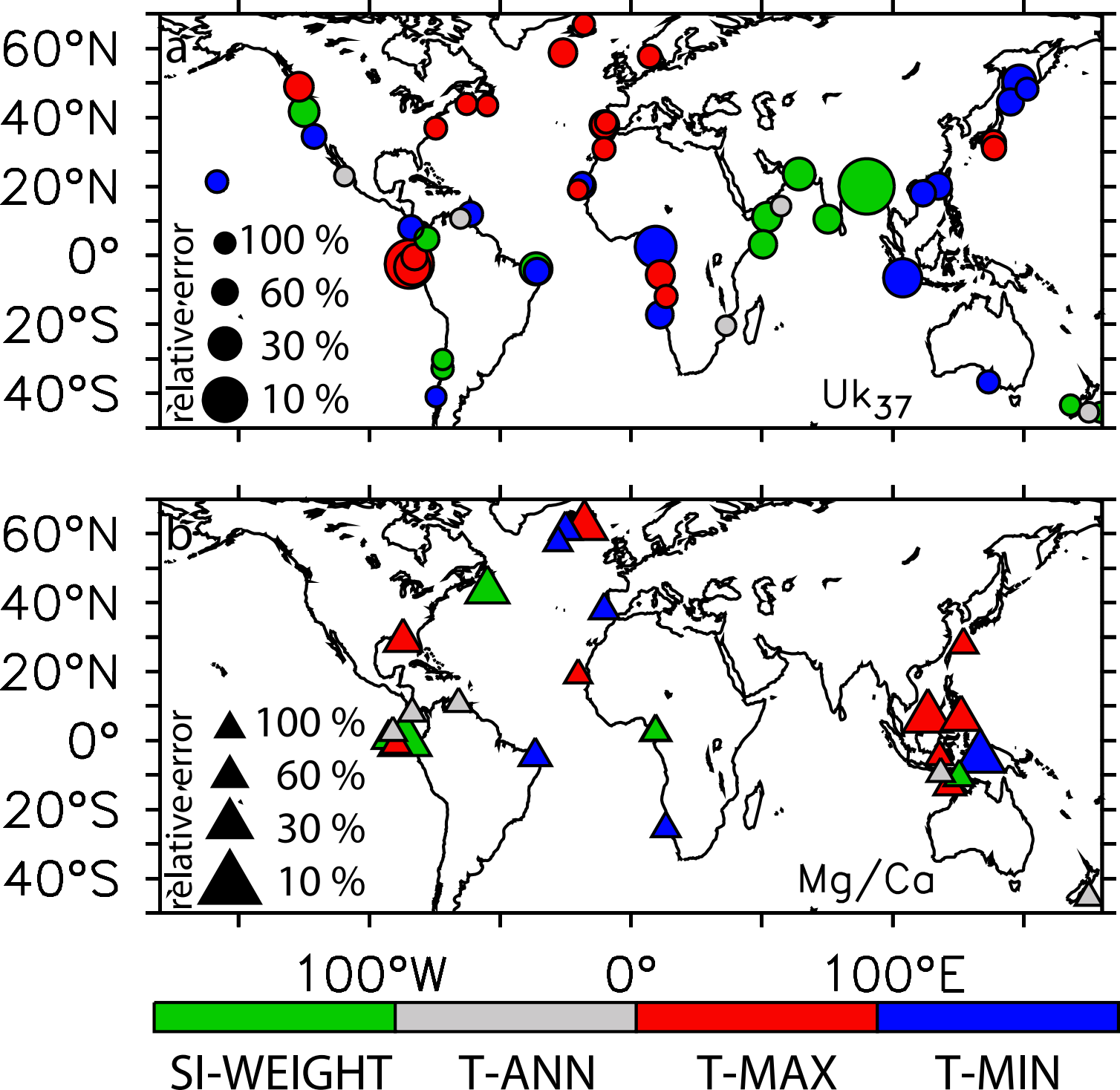
a
60°N
40°N
20°N
0°
20°S
40°S
relative error
100 %
60 %
30 %
10 %
Uk37
b
60°N
40°N
20°N
0°
20°S
40°S
relative error
100 %
60 %
30 %
10 %
Mg/Ca
100°W
0°
100°E
SI-WEIGHT
T-ANN
T-MAX
T-MIN

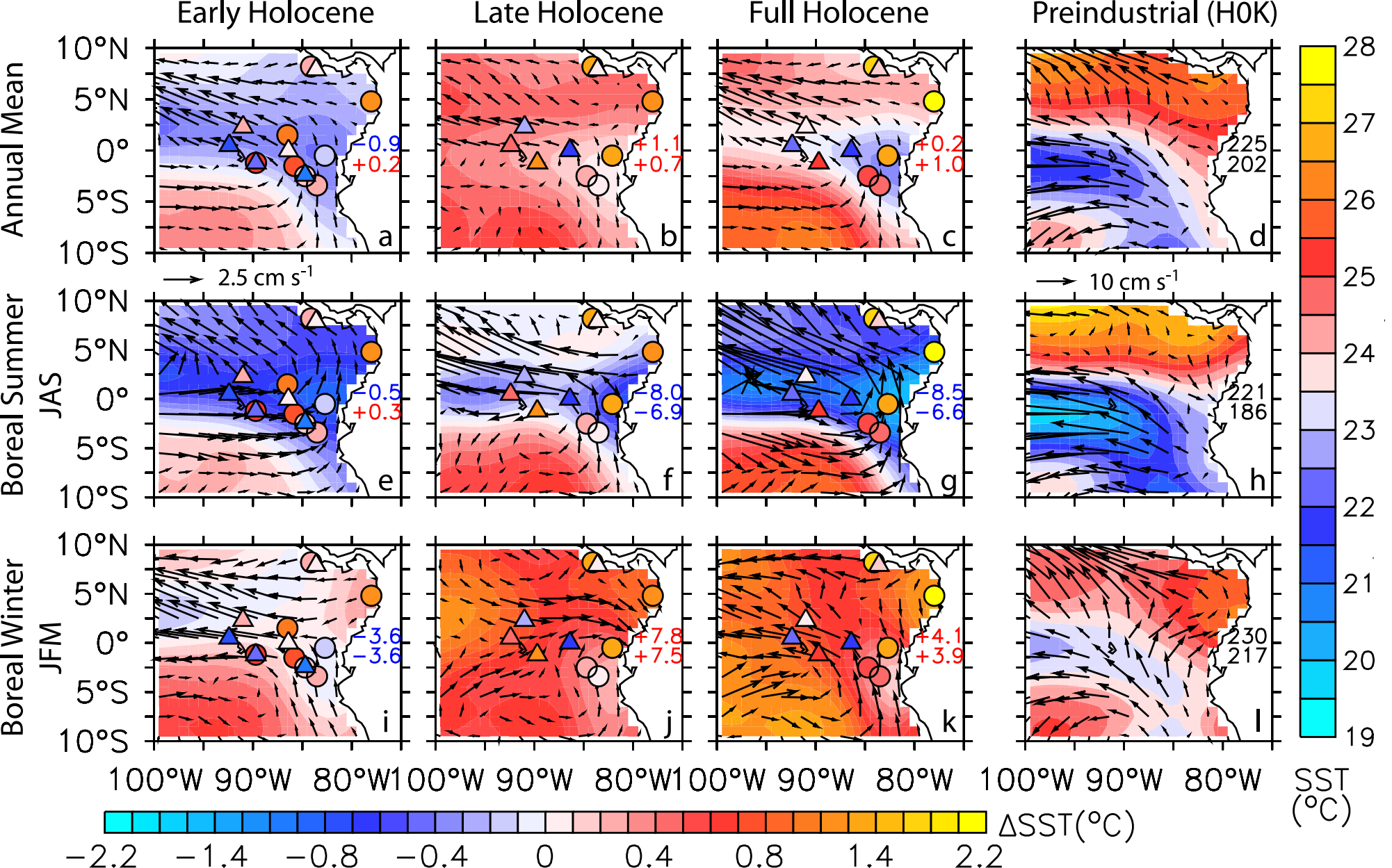
Early Holocene
Late Holocene
Full Holocene
Preindustrial (H0K)
Annual Mean
Boreal Summer
JAS
Boreal Winter
JFM
10°N
5°N
0°
5°S
10°S
2.5 cm s-1
10 cm s-1
0.9
+0.2
+1.1
+0.7
+0.2
+1.0
225
202
−0.5
+0.3
−8.0
−6.9
−8.5
−6.6
221
186
−3.6
−3.6
+7.8
+7.5
+4.1
+3.9
230
217
a
b
c
d
e
f
g
h
i
j
k
l
100°W 90°W 80°W
28
27
26
25
24
23
22
21
20
19
SST
(°C)
ΔSST(°C)
−2.2 −1.4 −0.8 −0.4 0 0.4 0.8 1.4 2.2

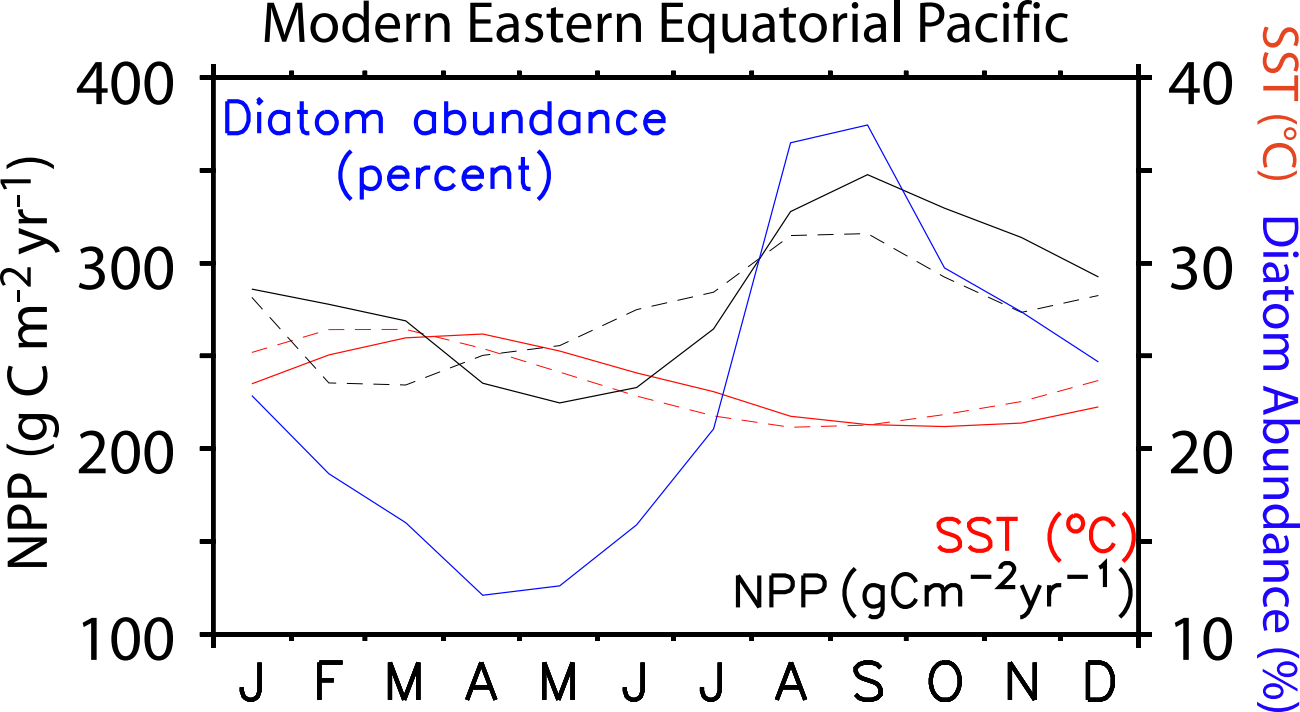
Modern Eastern Equatorial Pacific
Diatom abundance
(percent)
SST (°C)
NPP (gCm^{-2}yr^{-1})
NPP (g C m^{-2} yr^{-1})
SST (°C) Diatom Abundance (%)
400
300
200
100
40
30
20
10
J F M A M J J A S O N D

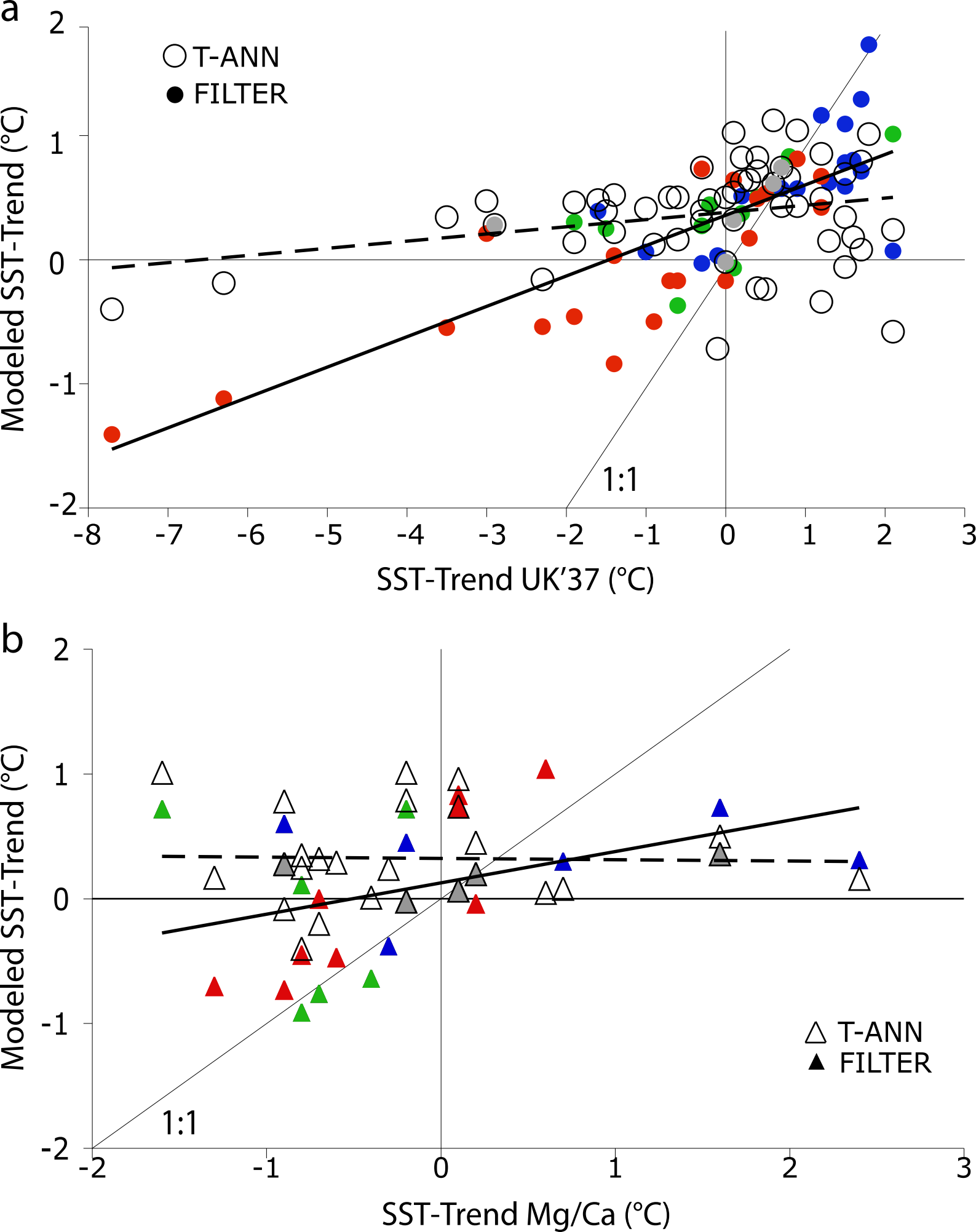
a
T-ANN
FILTER
1:1
Modeled SST-Trend (°C)
SST-Trend UK'37 (°C)
b
T-ANN
FILTER
1:1
Modeled SST-Trend (°C)
SST-Trend Mg/Ca (°C)